Hydrological Dynamics of the Congo Basin from Water Surfaces based on L-Band Microwave

Christophe Fatras, Marie Parrens, Santiago Peña Luque, Al Bitar Ahmad

AGU ADVANCING EARTH AND SPACE SCIENCE

Water Resources Research

RESEARCH ARTICLE
10.1029/2020WR027259

Special Section:
Advances in remote sensing, measurement, and simulation of seasonal snow

Hydrological Dynamics of the Congo Basin From Water Surfaces Based on L-Band Microwave

C. Fatras[1], M. Parrens[1,2], S. Peña Luque[3], and A. Al Bitar[4]

[1]CESBIO, Université de Toulouse, CNES/CNRS/IRD/UPS, Toulouse, France, [2]Université de Toulouse, INRAE, INPT, INP-PURPAN, UMR DYNAFOR, Castanet-Tolosan, France, [3]Centre National d'Etudes Spatiales, CNES, Paris, France, [4]Centre National de Recherche Scientifique, CNRS, Paris, France

Key Points:

- New knowledge of the Congo River Basin hydrology for the last decade through a new temporal and spatial dynamic water surface extent data
- The water extent in the Congo River Basin ranges from 78,602 to 99,225 km^2 between 2011 and 2017
- The lags between rainfall and flood in the nine Congo subbasins has a high variability ranging from 0 to 67 days

Correspondence to:
C. Fatras,
fatrasc@cesbio.cnes.fr

Citation:
Fatras, C., Parrens, M., Peña Luque, S. & Al Bitar, A. (2021). Hydrological dynamics of the Congo basin from water surfaces based on L-band microwave. *Water Resources Research*, *56*, e2020WR027259. https://doi.org/10.1029/2020WR027259

Received 4 APR 2020
Accepted 22 NOV 2020

Abstract In this study, the hydrological dynamics of the Congo River Basin (CRB) have been analyzed. This is achieved using multiangular and dual-polarization passive L-band microwave signal from the Soil Moisture and Ocean Salinity (SMOS) satellite to estimate water surface extent dynamics from 2010 to 2017. The results provide new insights into the poorly characterized wetlands, peatlands, and floodplains dynamics of the CRB. We found that the mean flooded area for the entire CRB is equal to 89,408 ± 20,623 km^2 corresponding to 2.39% of the entire basin. The results were compared with three land cover maps (European Space Agency-Climate Change Initiative [ESA-CCI], International Geosphere-Biosphere Programme [IGBP], and Global Surface Water Occurrence [GSWO]) and the SWAMPS global dynamic water surfaces product. More inland waters were detected than the four previous products, except along the rivers. Floods and droughts during the last 10 years were also depicted. The knowledge about the CRB hydrological behavior was improved by analyzing the date of maximum floods, the time lag in days between precipitation, water surface extent, and river water height at the outlet of the nine major Congo subbasin. A lag of 67 ± 3 days between rainfall and inundated areas was found in the Upper Congo ($r = 0.89$). In the Kasai subbasin, no time lag between rainfall and inundation was found ($r = 0.86$). The contribution of each floodplain to the Congo discharge was also evaluated. In the future, the fusion of the current surface waters with water heights from the SWOT mission can provide further information to the water volumes of the CRB floodplains.

Plain Language Summary The Congo River Basin (CRB) has a vast flooded area, that is poorly characterized. We developed new flood extent maps for the CRB based on satellite data in the L-band spectral band. This enabled an unprecedented insight into water dynamics of the wetlands, peatlands, and floodplains of the CRB through the detection of the dates of maximum floods, the lag with the rainfall peaks, and the duration of floods even in vegetated areas.

1. Introduction

The Congo River Basin (CRB) is the world's third largest in size (around 3.7 million km^2—Laraque et al., 2001, 2009), the second in terms of discharge after the Amazon basin (around 40,600 m^3 s^{-1} annual average—Becker et al., 2018). It contributes roughly up to 3.5 mm/yr of the global sea level variations (Beighley et al., 2011). The CRB contains also the second largest contiguous tropical rainforest in the world and plays a crucial role as a sink of CO_2, storing around 50 billion tons of carbon (Verhegghen et al., 2012). Dargie et al. (2017) reported that the "Cuvette Centrale," which represents around 30% of the entire basin, is the most extensive peatland in the tropics storing around 30.6 petagrams of carbon below ground (Dargie et al., 2019). This peatland is particularly vulnerable to land use and water cycle changes. Economic activities such as fisheries and agriculture impact about 80% of the population living in the CRB region (Bele et al., 2010). Thereby, this region is commonly judged as vulnerable to climate variations and extreme weather events such as droughts and floods (IPCC, 2007). However, there is considerable uncertainty in the projections of future rainfall change over the CRB from the Coupled Model Intercomparison Project (CMIP5) under the high-emissions experiment (RCP8.5) (Creese & Washington, 2016). Authors found that coupled global climate models can differ in their climatological mean rainfall by up to a factor of five in some months, with the largest differences in December (i.e., during the dry season in the equatorial and northern parts of the basin). Thus, it is crucial to improve our knowledge of the past and present water cycle in the CRB to reduce these uncertainties. The poor understanding of the CRB hydroclimate processes can be

shown by the number of associated scientific studies. Alsdorf et al. (2016) counted only 33 publications in peer-reviewed papers in Hydrology or Earth Science journals concerning the CRB and 299 concerning the Amazon basin. A key reason for this difference is the lack of available climate observations from the region, especially since the 1980s with increasing difficulties to access the CRB. For example, there were around 60 rain gauges in 1950 and only <10 in the 2000s (Washington et al., 2013). One way to access the climate and hydrological variables in the CRB is to use remote sensing data.

In this study, we focus on the temporal and spatial dynamics of the water surface extent over the CRB retrieved by satellite data during the last decade and their link to other major components of the hydrological cycle namely rainfall and river flow. Water surface extent corresponds to open water surface in lakes, rivers, wetlands, peatland, floodplains, and human-made reservoirs. This variable is a key component of the land water budget. In interaction with both ocean and atmosphere, it plays a key role in the Earth's climate variability. Wetlands and floodplains are also the place of carbon and methane emissions to the atmosphere (Abril et al., 2014; Richey et al., 2002) and brittle ecosystem sheltering biodiversity (Silva et al., 2013).

Advances on remote sensing led to the development of several water surface extent products at global scale. For example, Pekel et al. (2016) used three million Landsat images (optical sensor) to provide a high-resolution map of surface water extent. The most important limitation of the optical sensors is their inability to probe through clouds and dense vegetation cover, which is essential in tropical wet regions like the CRB. Using data fusion from several sensors: passive microwave (e.g., Special Sensor Microwave/Imager [SSM/I]), active microwave (European Remote Sensing satellite [ERS]), and optical sensors (Advanced Very High-Resolution Radiometer [AVHRR]), Prigent et al. (2001) developed the Global Inundation Extent from Multiple Satellites (GIEMS) product. It provides monthly global maps of inundation data at 25 × 25 km spatial resolution from 1993 to 2007 (Papa et al., 2008). Recently, the coarse resolution, Surface Water Microwave Product Series (SWAMPS), has been developed from the fusion of passive and active microwave sensors (SSM/I, SSMIS, ERS, QuikSCAT, ASCAT) and visible sensors (MODIS) (Schroeder et al., 2015). The GIEMS and SWAMPS data sets have been compared in Pham-Duc et al. (2017) showing that GIEMS dynamics are more consistent with other hydrological variables such as the river discharge. Detection of inundated surfaces generated by hurricane Irma and Harvey and using observations from the Cyclone Global Navigation Satellite System (CYGNSS) NASA mission was demonstrated in Chew et al. (2018). Lavalle et al. (2018) showed the ability of the CYGNSS observations to detect water surfaces in dense vegetation using a bistatic scattering modeling in L-band.

In recent years, some studies dealt with inland water in the CRB using remote sensing (Becker et al., 2018; Bwangoy et al., 2010; Jung et al., 2010; Lee et al., 2014, 2015; O'loughlin et al., 2013; Rosenqvist & Birkett, 2002) and/or modeling approaches (Munzimi et al., 2019; Revel et al., 2019; Tshimanga & Hughes, 2014). For example, Bwangoy et al. (2010) classified the wetlands in the Cuvette Centrale at high spatial resolution by using optical and radar data. Rosenqvist and Birkett (2002) detected the maximum of flood extent in the Central Congo by using Synthetic Aperture Radar from JERS-1 satellite. While providing valuable information on water extents, Bwangoy et al. (2010) and Rosenqvist and Birkett (2002) provide little insights on the temporal behavior of water surfaces. Becker et al. (2018) used the GIEMS product to estimate water surface dynamics in the CRB. Authors found that during the 1993–2007 period, the CRB water surface extent varied from 40,000 to 78,932 km^2 excluding the Tanganyika lake (around 32,600 km^2). However, some limitations for detecting inundation in dense vegetated areas were noted in the GIEMS product (Prigent et al., 2007) introducing a negative bias in the estimation of the water surface extent in the tropical basins. The recently developed Surface WAter Fraction (SWAF) product aimed at mapping water surface extent dynamics over the Amazon basin from 2010 to present (Parrens et al., 2017). Inland waters are monitored every 3 days at 25 × 25 km spatial resolution. Besides the high temporal resolution, the significant advantage of the approach is its ability to detect water under dense vegetation by using the L-band passive microwave frequency from the Soil Moisture and Ocean Salinity (SMOS) mission (Kerr et al., 2001). The analysis of the hydrological regime of the Congo river subbasins in this study relies on an improved algorithm for the SWAF product by including multiangular and dual-polarization acquisitions to determine soil, forest, and water contributions. The present study aims at contributing to a better understanding of the water surface dynamics and hydrological processes in the CRB during the last decade. In the next sections, the CRB hydrology is described, followed by the used data sets and methods. The results focus on analyzing the hydrological

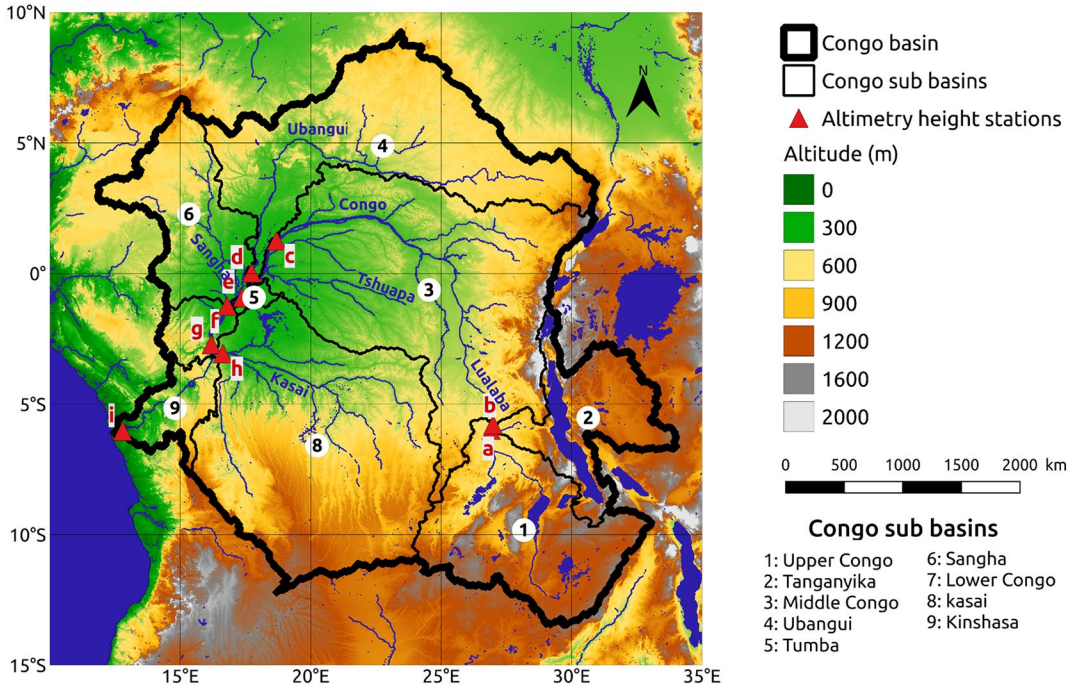

Figure 1. Geography of the CRB. Base map corresponds to the altitude in meters, over which are overlaid the main rivers (blue lines), the borders of the CRB (thick black line), the delimitations of the nine subbasins (black lines), and the altimetry height stations at the subbasin outlets (red triangles). CRB, Congo River Basin.

dynamics of the CRB from the open water surface perspective. The water dynamics are compared to existing water surface products, river levels, rainfall. The discussion section places the results of water extents in the context of existing recent studies over CRB.

2. Area of Study

The CRB hydrological basin spreads over 10 African countries (Angola, Burundi, Cameroon, Central African Republic, Democratic Republic of Congo, Republic of Congo, Rwanda, South Sudan, Tanzania, and Zambia). It extends over 3.705 million square kilometers (Lehner et al., 2008). From the east-African rift the Congo-Lualaba-Chambeshi river system flow over 4,700 km toward the Atlantic Ocean. The wetland areas in CRB include flooded forests and inundated grasslands, both characterized by vegetation adapted to water saturated soils, anaerobic conditions, and frequent flooding. Flooded forests cover large areas in the center of the study site, mainly in the western part of the Democratic Republic of Congo and the northeastern part of the Republic of Congo (Bwangoy et al., 2010; Mayaux et al., 2000). This region is called the Cuvette Centrale, and includes the CRB peatlands that are the main carbon sink of the CRB (Dargie et al., 2019). They are temporarily or permanently inundated, and in all cases characterized by soils with poor drainage (Mayaux et al., 2002). The CRB can be divided into nine subbasins based on the HydroSHEDS basin data set (Figure 1). Details of the area, altitude, cover type, and slopes for each subbasin are provided in Table 1. The CRB includes four major lakes: the Tanganyika lake in the eponym subbasin, the Kivu lake at the North of the same subbasin, the Tumba lake in the subbasin of the same name, and the Mai-Ndombe lake in the North of the Kasai subbasin. Along these four main lakes, we can also consider the Bangweulu, Mweru, and Kabamba lakes in the Upper Congo subbasin that form a hydrologic network at the source of the Congo river (Chambeshi river).

The annual mean temperature over CRB is about 25°C. The difference between the temperature of the warmest month (March) and the coldest month (July) is of 2°C (Bultot, 1974). The annual rainfall is ~1,900 mm/yr along an east-west trend across the basin, decreasing northward and southward to ~1,100 mm/yr (Alsdorf, 2016). The northern part of the basin experiences a minor rainy season from Sep-

Table 1
Characteristics of Each Congo River Basin (CRB) Subbasin

Subbasin name	Surface area (km^2)	Min altitude (m)	Max altitude (m)	Mean altitude (m)	Forest (%)	Ground and sparse vegetation (%)	Mean slope (°)	STD slope (°)
Upper CRB	453,078	548	1,967	1,135	77.00	18.40	2.16	3.07
Tanganyika	266,511	551	3,071	1,164	52.97	33.03	3.28	5.15
Middle CRB	973,778	295	3,183	603	85.60	13.60	3.33	3.83
Ubangui	648,276	295	1,719	611	84.95	14.57	2.19	1.84
Tumba	14,083	289	404	323	80.35	7.95	1.31	1.36
Sangha	285,043	287	1,956	522	89.87	9.79	2.88	2.52
Lower CRB	67,658	272	831	465	54.92	42.65	3.96	4.27
Kasai	894,489	272	1,492	745	83.42	15.83	3.47	3.58
Kinshasa	102,307	1	1,319	520	43.49	54.19	4.86	4.56

The forest land cover and the ground and sparse vegetation land cover are extracted from the European Space Agency-Climate Change Initiative land cover product (see Section 3.3.3 for product description). Mean and STD of the slopes were calculated from SRTM data.

tember to November and a major one from the first half of March to early May. In the southern part of the basin, the minor rainy season lasts from February to May and the major rainy season occurs between September and December (Samba et al., 2008).

The Congo river discharge varies strongly across the year (Alsdorf et al., 2016), with high discharge in November-December and low discharge in July-August. At the city of Kinshasa, close to the outlet of the entire CRB, Vanden Bossche and Bernacsek (1990) shows a discharge variation between 23,000 and 75,000 m^3/s, with an average value at 41,200 m^3/s. This average value is coherent with the discharge of 40,662 m^3/s provided in Alsdorf et al. (2016), and with the average river flow from a century of data from 1902 to 2010 determined at 40,612 m^3/s (Laraque et al., 2013a).

3. Materials

3.1. Data Sets for the L-Band Water Surface Retrievals

3.1.1. L-Band Passive Microwave

Earth observation from space in passive L-band has emerged in the last decade by the launch of the SMOS satellite from ESA in 2010 and more recently in 2015 by the launch of the SMAP satellite from NASA. The SMOS mission is a joint program of the European Space Agency (ESA), the French Space Agency (CNES), and the Spanish Centro para el Desarrollo Tecnologico Industrial (CDTI) in the framework of the Earth Explorer Opportunity Mission initiative. It observes using a 2D interferometric radiometer in passive microwave at 1.4 GHz (L-band). The satellite is in Sun-synchronous orbit with a 06:00 LST ascending equator crossing time and a 18:00 LST descending equator crossing time. The globe is fully imaged twice every 3 days. The radiometric product from SMOS is the brightness temperature (TB). This signal is highly sensitive to the water in the first centimeters of the soil (Kerr et al., 2001). Clouds and rain have a negligible effect on the signal (Ulaby, 1982) and the atmospheric contribution is limited and well known (Kerr et al., 2012). The microwave signal is to a lesser extent sensitive to the vegetation, with L-band frequency being less impacted by the vegetation than higher frequencies (Ulaby, 1982). The SMOS mission provides multiincidence-angle observations at full polarization. In this study, the SMOS Level (L) 3 TB (RE04v300) (Al Bitar et al., 2017) produced by the Centre Aval de Traitement des Données SMOS (CATDS) are used. These data are projected on the Equal-Area Scalable Earth (EASE) Grid version 2 with a spatial resolution of 25 × 25 km at 30° latitude. The main features of the SMOS L3 TB are: (i) the L3 TB for horizontal (H) and vertical (V) polarizations are expressed at the top of the atmosphere over the terrestrial reference frame; and (ii) they are bin averaged every 5° from 2.5° to 62.5°. In the present study, SMOS L3 TB are used from 2011

to 2017 over the Congo Basin. Angles of 32° ± 5°, 40° ± 5°, and 47° ± 5° in both horizontal (H) and vertical (V) polarizations are considered to retrieve the water fraction over the tropical basin.

3.1.2. Skin Temperature

The surface skin temperature produced by the European Centre for Medium-range Weather Forecasting (ECMWF) was used in this study. They were obtained from the SMOS L3 preprocessor, which computed the spatiotemporal interpolated weather data from the ECMWF reanalysis products over the EASE 2.0 grid at the time of revisit of the SMOS satellite.

3.1.3. Land Cover Maps

The Globe Cover product from the International Geosphere-Biosphere Programme (IGBP) were used as land cover. The IGBP land cover map is obtained using images from the Moderate Resolution Imaging Spectroradiometer (MODIS) with a spatial resolution of 0.005° covering years 2001–2012 (Broxton et al., 2014; Friedl et al., 2010). After projection over the EASE2.0 grid, the forest classes were used to determine the forest contribution on the total SMOS TB. The latest release of the ESA Climate Change Initiative (CCI) land cover map was also used (Bontemps et al., 2013). The water/no-water global mask at 150 m is built using Synthetic Aperture Radar (SAR) data in combination to Landsat-derived products from years 2003 to 2012. Data were downloaded from http://www.esa-landcover-cci.org/. From the 37 classes provided, we used in this study the five classes related to water areas—that is, water bodies, cropland irrigated, or postflooding, tree cover flooded fresh or brackish water, tree cover flooded saline water, and shrub or herbaceous cover flooded fresh/saline/brackish water.

3.2. Comparison Data Sets

The comparison data sets are used for two objectives. First to indirectly access the accuracy, physical soundness, and spatial coherence of the retrieved water surface fractions. Second to link several components of the water cycle (precipitation, flooded area, and water height) of the CRB subbasins. In the study, only open access data were selected for the comparison.

3.2.1. Water Surface Extent Maps

Four water fraction products were considered for the comparison:

- The Global Surface Water Occurrence (GSWO) data set consists in global occurrence of inundated area at 30-m resolution over the 1984–2013 period (Pekel et al., 2016). This data set has been obtained from the processing of the entire archive of optical data from the Landsat 5 Thematic Mapper, the Landsat 7 Enhanced Thematic Mapper-plus and the Landsat 8 Operational Land Imager. The data are available at https://global-surface-water.appspot.com/. The GSWO was resampled over the EASEv2 25 km for the comparison
- The classes corresponding to water bodies extracted from the IGBP land cover map described in Section 3.1.3
- The classes corresponding to water bodies extracted from the ESA CCI land cover map
- The SWAMPS data provided daily surface water globally at 25-km resolution from 1992 to 2013. This product is based on the combination of passive and active microwave sensors (SSM/I, ERS, QuikSCAT, and ASCAT) and visible sensors (MODIS) (Schroeder et al., 2015). In our study, data from 2010 to 2013, coinciding with SMOS data availability over the CRB, were considered and averaged over the 4 years

For each of the four products, the water classes were aggregated and resampled to obtain the water fraction (%) present in each cell of the EASE v2.0 grid.

3.2.2. Altimetry Data

The flood extent variations over time are compared with water height values from satellite altimetry for each subbasin outlet (Figure 1). The water level time series (in meters) for each virtual station over the 2011–2017 time period were downloaded from the Hydroweb database (http://hydroweb.theia-land.fr/). The water level computation method and the location of the virtual stations are presented in Da Silva et al. (2010). The Jason altimeter series, in particular Jason-2 and Jason-3, and Sentinel-3 are selected. The Jason series

operate at Ku-band (13.575 GHz) and C-band (5.3 GHz) and have a revisit period of ~9.9 days (Birkett & Beckley, 2010). Jason-2 was launched in 2008 and ended operations in 2019. Jason-3 was launched on January 2016. The first Sentinel-3A altimetry satellite (Donlon et al., 2012) was launched on February 2016, it operates at Ku-band (13.575 GHz) and C-band (5.41 GHz). It consists as of December 2019 of two satellites (Sentinel-3A and -3B). Worth noting that the available Jason-1/2/3 virtual stations over the Sangha and Lower Congo subbasins were far from the outlets and were not considered in the analysis. Only Sentine-3A data from 2016 to 2019 were used for these two basins.

3.2.3. Precipitation Data

The 3B42 TRMM v7 daily rainfall data are used with a spatial resolution of 0.25 × 0.25. This data set is obtained by combining satellite information from the passive Tropical Microwave Imager (TMI) and Precipitation Radar (PR) onboard the Tropical Rainfall Measuring Mission (TRMM), a Japan—US satellite launched in November 1997, and the Visible and InfraRed Scanner (VIRS) onboard the Special Sensor Microwave Imager (SSM/I) (Huffman et al., 1995, 2007). It is available on the Goddard Earth Sciences Data and Information Services Center (GES DISC) website: http://daac.gscf.nasa.gov. Over the CRB, large differences between the precipitation data based on satellite observations have been noticed. The TRMM data were identified as the most coherent with the observed gauged river discharge (Alsdorf et al., 2016).

4. Surface WAter Fraction Determination From L-Band to SWAF

4.1. Retrieval Algorithm

The methodology presented in Parrens et al. (2017) has been extended and adapted to the CRB particularities. In the previous version, only contributions from forested and water surfaces were considered. In the case of the CRB, there is need to consider contributions from water, forest, and soil surfaces because the CRB exhibits more complex land cover patterns than the Amazon. In fact, the observed area in the CRB encompasses more different kinds of grounds than in the Amazon. Indeed, whereas the Amazon can be modeled as either water or tropical forest, the Congo River Basin has >40% of its total area being croplands and natural vegetation mosaics. The use of the algorithm presented in Parrens et al. (2017) over the CRB was unsatisfactory due to this complex mosaic of grounds, with a large overestimation of water surfaces in the areas outside forests for all polarization and incidence angle. In terms of brightness temperature, the signature of the soil and the forested surfaces is quite different (Ulaby, 1982). From Fresnel's law, it is clear that a better detection of water surface extent (with or without vegetation) can be obtained using dual-polarization and multiangular TB contributions. This is an essential modification to better characterize the spatial heterogeneity of the CRB. Here, by we consider that for a given scene, the brightness temperature (TB) at the top of atmosphere (TOA) as the sum of the elementary contributions from forest, soil, and water surfaces

$$TB_{TOA}\left(q,p\right) = F_W\left(q,p\right) + F_s \times TB_{SOIL}\left(q,p\right) + F_F \times TB_F\left(q,p\right) \quad (1)$$

where $\boldsymbol{TB_{TOA}}$ is the TB at top of atmosphere in Kelvin (K) which should corresponds to the TB observed by SMOS after correction of the Faraday and geometric rotation, $\boldsymbol{TB_W}$ is the modeled water TB (K), $\boldsymbol{TB_{SOIL}}$ is the soil TB (K), $\boldsymbol{TB_F}$ is the forest TB (K). $\boldsymbol{F_W}$, $\boldsymbol{F_S}$, and $\boldsymbol{F_F}$ are the corresponding surface fractions (with $\boldsymbol{F_W + F_S + F_F = 1}$); $\boldsymbol{q}$ stands for the incidence angle index and $\boldsymbol{p}$ for the polarization index (H or V).

An overview of the SWAF algorithm is presented in Figure 2. To be able to determine more precisely the Surface WAter Fraction in the whole CRB, we introduced a soil component with a localized soil brightness temperature to represent either vegetation or croplands. To diminish the possible misdetections and dispose of the variations in the TB due to low vegetation cover, the use of an equation system with different polarizations and angles is proposed in this study. Various equation systems were tested against only one in the former algorithm (1–2 polarizations, 1–2–3–4 incidence angles). The best results in terms of spatial cover and preciseness were obtained using an equation system with two polarizations and three incidence angles, hence the use of a six equations system. This configuration is the one presented in this study, using both H and V polarization, and 32.5°, 40°, and 52.5° incidence angles, and that for the ascending orbit (less RFI probability compared to descending orbit). The outputs of the SWAF algorithm are the estimated water

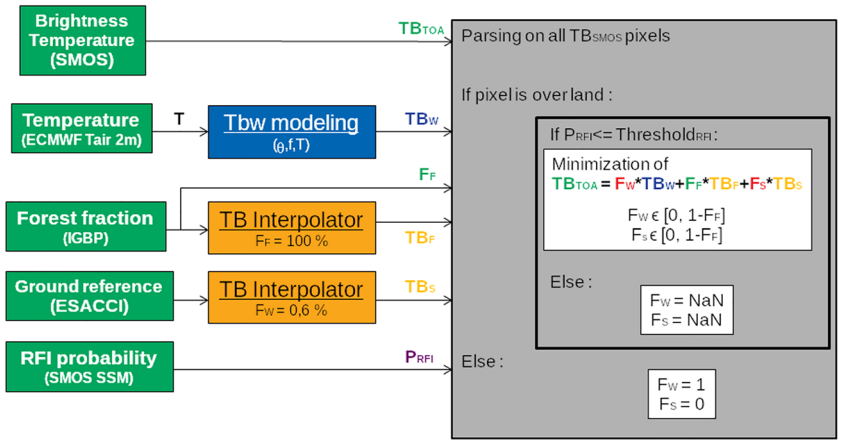

Figure 2. Scheme of the Surface WAter Fraction retrieval algorithm.

($\boldsymbol{F_W}$) and soil ($\boldsymbol{F_S}$) fractions (in red). The prior forest fraction $\boldsymbol{F_F}$ is set from the IGBP forest fraction. The inputs (TB L3 SMOS, ESA-CCI, IGBP, ECMWF) are presented in green, the modeled TB in blue, and the ancillary data are in purple. Unauthorized emissions in L-band from the ground can induce Radio Frequency Interference (RFI) (Soldo et al., 2015). For this reason, the TB is filtered when the RFI probability exceeds 25%. The orange values in Figure 2 correspond to the interpolated values of $\boldsymbol{TB_F}$ and $\boldsymbol{TB_S}$, see next section). $\boldsymbol{TB_W(q,p)}$ is modeled using the Klein and Swift (1977) model based on the parameterization in Ulaby (1983) and using the physical skin temperature from ECMWF of the closest water body. The frequency, angle, polarization, and physical temperature of the water surface are required for the $\boldsymbol{TB_W}$ modeling. $\boldsymbol{F_W}$ and $\boldsymbol{F_S}$ are constrained in the inversion process to the interval $\mathbf{[0, 1 - F_F]}$. An iterative minimization scheme of the sum of quadratic differences between modeled and SMOS $\boldsymbol{TB_{TOA}}$ over polarizations and angles is applied to retrieve $\boldsymbol{F_W}$ and $\boldsymbol{F_S}$.

4.2. Reference Forest and Soil Brightness Temperatures

In order to provide the SWAF algorithm with a representative and updated forest reference brightness temperature, the observed TB for each pixel with a 100% forest cover is interpolated from the IGBP land cover. The forest reference $\boldsymbol{TB_F}$ matrix is updated for every SMOS acquisition for each couple of polarization and incidence angle.

A similar approach is applied for the reference soil TB ($\boldsymbol{TB_S}$) where only permanently nonflooded areas are considered using a threshold on the land cover map to obtain a "soil reference map." The map consists in the fusion of five classes from ESA-CCI land cover map—that is, water bodies, cropland irrigated or postflooding, tree cover flooded fresh or brackish water, tree cover flooded saline water, and shrub or herbaceous cover flooded fresh/saline/brackish water—corresponding to the maximum theoretical flood extent. A threshold at 0.6% provided good performance on the SWAF estimation without being too restrictive.

4.3. Postprocessing

The retrieved water fraction is obtained over the L3TB daily product, which is constituted of ascending or descending TB over the swath, since the satellite provides a 3-days global coverage. To obtain a continuous water fraction map, a linear interpolation for each pixel independently. In the case of the CRB, the water surface was not retrieved over the minimum extents of the Tanganyika lake.

5. Results

The following calculations were computed using the two H and V polarization and three incidence angles (32.5°, 40°, and 52.5°) for the ascending orbit. Those values allowed the best compromise between angle discrimination, water detection estimation, satellite swath width, and RFI detection.

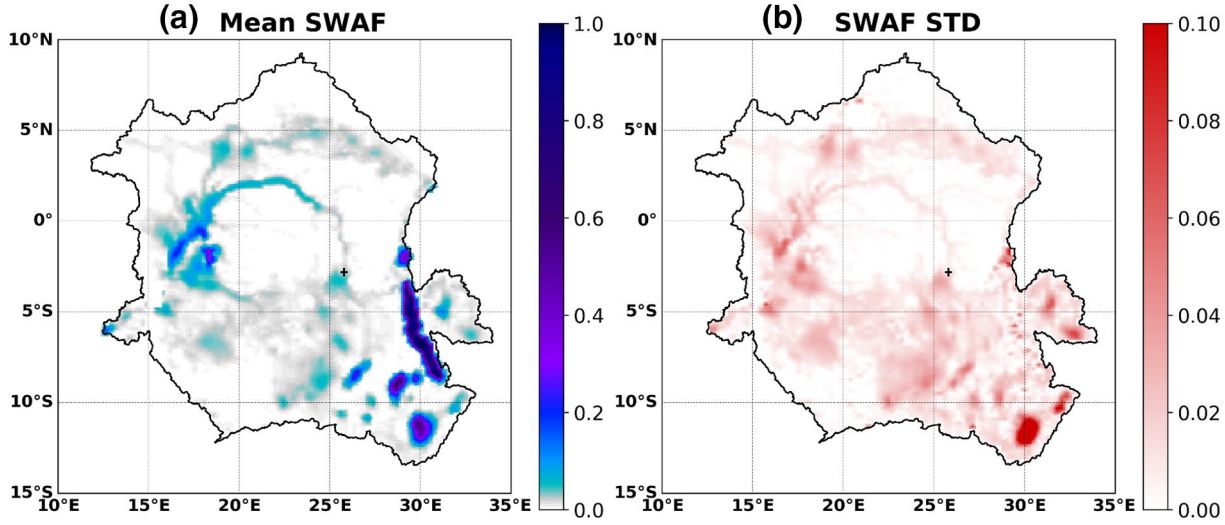

Figure 3. Mean and standard deviation maps of Surface WAter Fraction for the 2011–2017 time period. The black cross indicates the location of the Kindu city.

5.1. Water Surface Extent Maps

Daily water fraction maps were computed over the entire CRB during the 2011–2017 period. The calculation of the mean and standard deviation (STD) values for each pixel during the entire time period is provided in Figure 3. The main river and lake network (Congo, Kasai, Lualaba, Ubangui, Sangha rivers, and Tanganyika, Bangweulu, Mweru, Kivu, Kabamba, Tumba, Mai-Ndombe lakes) can be depicted in the mean SWAF map (Figure 3a). The mean flooded area for the CRB is found to be about 89,408 km^2 (2.39% of the entire basin). Significant flood areas can be distinguished in the eastern part of the Ubangui subbasin and the eastern part of the Kasai subbasin.

The SWAF STD map shows up to 0.1 variability of the water fraction values over the period at the scale of 625 km^2. The mean STD for the whole basin is about 9.2×10^{-3}. In particular, the Bangweulu lake showed an important variation of the water fraction (STD > 0.2). Another area that showed a significant variation of water surface are the Cuvette Centrale area and the Kasai subbasin with an STD up to 0.06.

The monthly mean water fraction over the 2011–2017 period is shown in Figure 4. A maximum of total flooded area is identified in April with 99,225 km^2 (2.66% of total CRB), and a minimum in July with 78,602 km^2 (2.11% of total Congo area). This dynamic corresponds to a variation of 20,623 km^2 (0.55%). The dry season is observed in the southern part of the whole basin for June-July, and in the northern part during December-January.

In Figure 3, it is indicated the location of the Kindu city in the southern part of the Middle Congo subbasin, in the Maniema province (Lat: −2.95°, Lon: 25.91°). Kindu is located Northeast of a large floodplain (~15,000 km^2), which presents yearly floods from November to May (see Figure 4). This floodplain shows the sensitivity of the SWAF approach for the detection of yearly flood cycles.

5.2. Identification of Extreme Events Over 2011–2017

For each subbasin, the flood extent time series has been plotted with the mean flood extent regime over the 2011–2017 period in the background as a reference (Figure 5). The flood extent has been smoothed using a Hanning filter of 31 days. This smoothing has not been applied to the mean flood extent regime. The difference between the flood regime and actual time series enables the depiction of flood and drought events. Hence, the 2014 extreme floods are observed in the Upper Congo, Tumba, Sangha, and Lower Congo subbasins. The winter 2015–2016 flood event is observed in the Tanganyika, Middle Congo, Tumba, and Kinshasa subbasins. The summer 2016 flood anomaly is detected on the Upper Congo, Tanganyika, Middle Congo, and Kasai subbasins. During 2017, the Ubangui, Sangha, and Lower Congo subbasins showed high flood

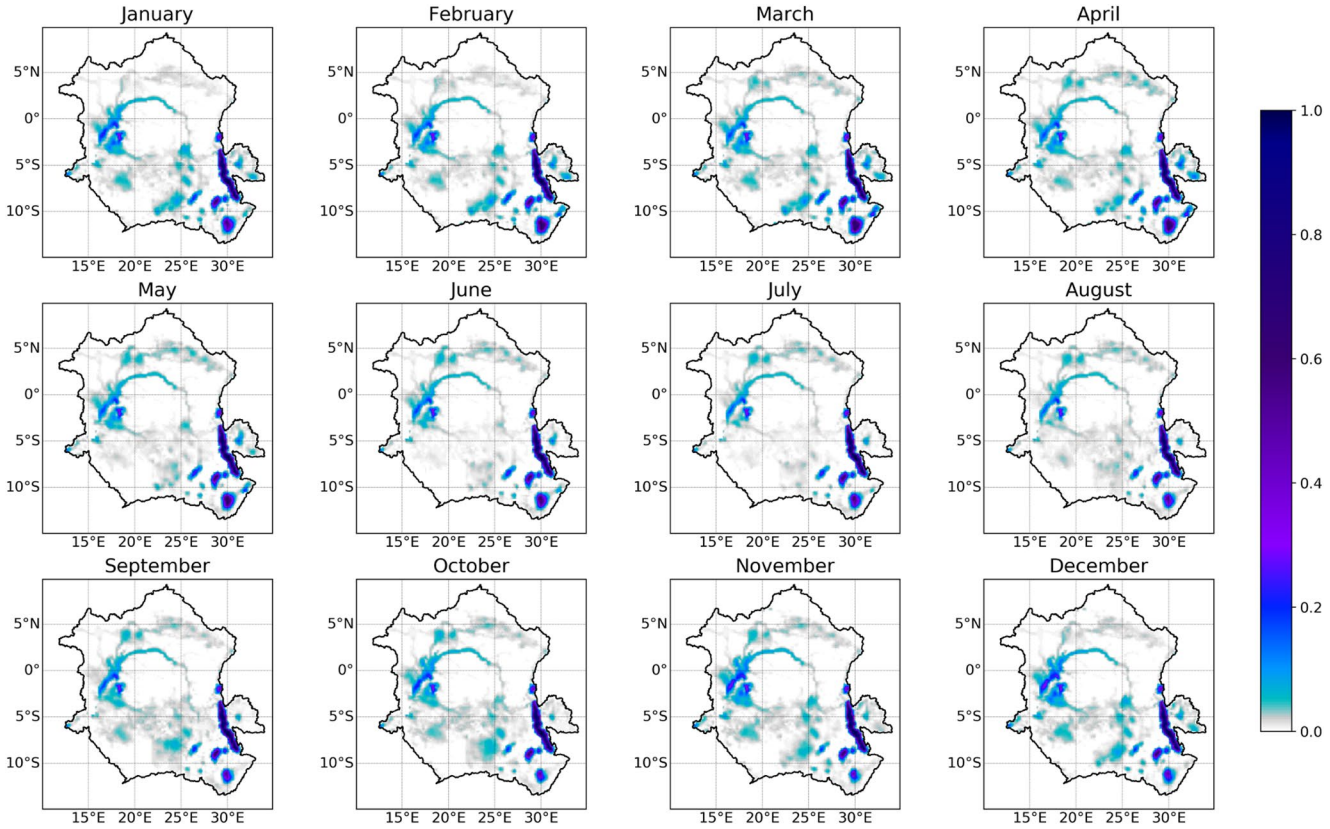

Figure 4. Monthly mean Surface WAter Fractions over the 2011–2017 time period.

extent. Drought anomalies are also observed in winters of 2011–2012, 2012–2013 and 2014–2015, 2015, and winter 2016–2017. The winter 2011–2012 drought anomaly is observed in the Kinshasa subbasin. The winter 2012–2013 drought is observed in the Sangha subbasin. The winter 2014–2015 drought is observed only for the Middle Congo subbasin. The drought of 2015 is observed in the Upper Congo and Tanganyika subbasins. The drought of winter 2016–2017 is observed in the Tumba, Sangha, and Lower Congo subbasins.

5.3. Comparison With Existing Water Surface Extent Maps

The mean water fraction map extracted from the SWAF algorithm has been compared with four water extent maps described in Section 3.2. For each pixel, the differences between the mean SWAF over the 2011–2017 period and each data set have been computed. Figure 6 shows the difference maps between SWAF and the other data sets along with the histograms of each data set over the CRB and over forest areas only. The SWAF algorithm shows higher total water surface extent compared with the other products: +13,763 km^2 more than GSWE, +18,788 km^2 more than ESA-CCI, +38,696 km^2 more than IGBP, and +43,135 km^2 more than SWAMPS (Table 2.).

Compared to GSWO and ESA-CCI maps, SWAF underestimates the water extent along the main rivers and the borders of the lakes. SWAF water fraction products detect more water surfaces under forests as shown in the histogram over the forest areas at low water fraction values (Figure 6f). SWAF detects more flood extent than the IGBP water map, except in the center of the small lakes and along the rivers. SWAF detects more water than SWAMPS in nearly all the cases yet small differences are identified over the Tanganyika lake borders. The histogram in Figure 6 shows that SWAF values are always higher than the SWAMPS values. SWAF is higher than IGBP for water fractions up to 0.5 and then lower for higher water fractions. SWAF is—despite a few exceptions—higher than GSWO and ESA-CCI values. This behavior is particularly marked for values between 0.6 and 0.8.

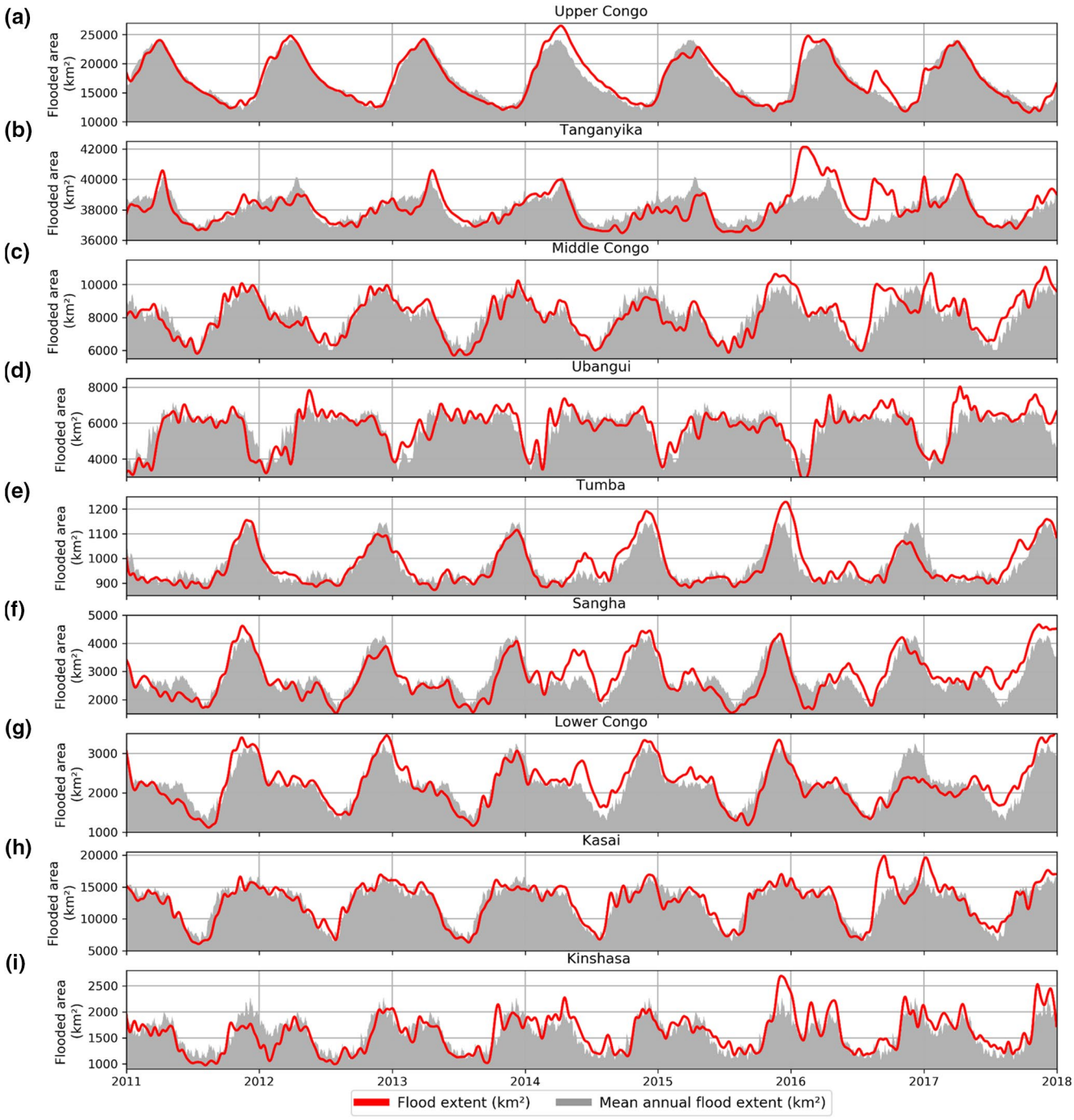

Figure 5. Time series of the total flood extent observed for each Congo subbasin (red) using SWAF algorithm. The mean annual flood extent over the 2011–2017 observation period is displayed in gray. SWAF, Surface WAter Fraction.

5.4. Hydrological Dynamics of the Congo Subbasins

For each subbasin, normalized cumulative rainfall, cumulative flood area, and normalized water heights at each subbasin outlet are plotted in Figure 7. Flood extent time series are in red and the normalized total rainfall from TRMM data for each subbasin in blue. Both flood extent and normalized rainfall time series have been smoothed using a Hanning filter (Harris, 1978) of 31 days. The water heights from altimetry are located at the closest virtual station to the outlet (black lines in Figure 7). The normalized water height time

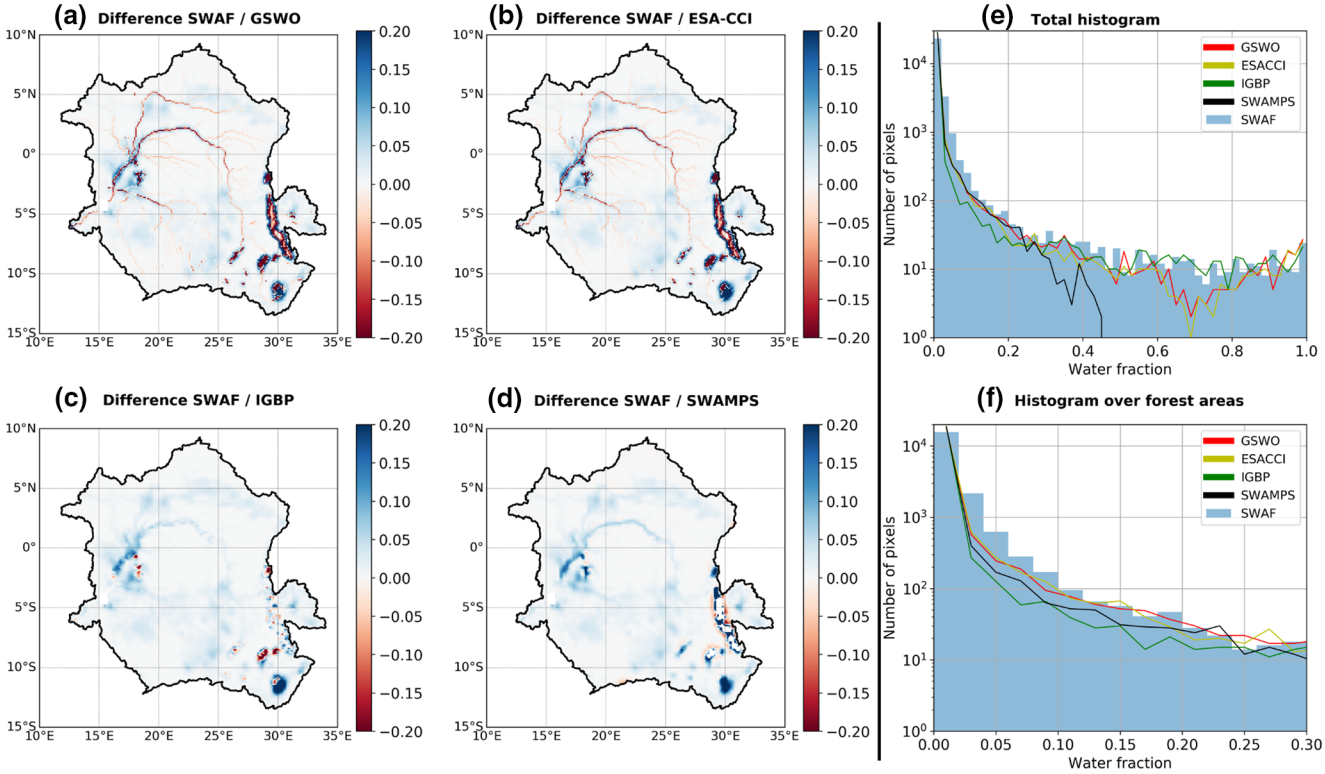

Figure 6. Difference between the mean SWAF map over the 2011–2017 time period and four other products: (a) GSWO extent; (b) ESA-CCI water bodies; (c) IGBP water bodies; and (d) SWAMPS mean water fraction over the 2010–2013 time period. And histogram of all the data sets: (e) over the whole Congo basin. (f) Histogram over the forest area of the Congo basin. CCI, Climate Change Initiative; ESA, European Space Agency; GSWO, Global Surface Water Occurrence; IGBP, International Geosphere-Biosphere Programme; SWAF, Surface WAter Fraction; SWAMPS, Surface Water Microwave Product Series.

series is short over the Sangha and Lower Congo subbasin (2016–2017) due to the lack of adequate virtual station with a long time series close to the outlet.

As expected from the hydrological cycle processes, a lag between the beginning of the rainy season and the flood extent peak can be noticed, along with a lag between flood extent peak and the water height level at the outlet of each subbasin. The lag values are reported in Table 3. The following comments can be given for each subbasin:

- The Upper Congo subbasin presents a high lag between rainfall and flood extent (67 days on average during the 2011–2017 period) with a correlation value equal to 0.89 when the lag is removed. This is due to the presence of lakes that act like a buffer for water flow. This buffer induces a lag between maximum water extent and water height at the outlet of 28 days (correlation with a lag of 28 days: 0.90).
- The Tanganyika subbasin flood extent variations are linked to large temporary ponds east of the main Tanganyika lake. The extent variations are correlated with the rainfall regime ($r = 0.7$) with low lag (~26 days). We also observe a good correlation between the flood maximum extent and water height (lag of ~5 days, $r = 0.68$).
- The Middle Congo subbasin presents a bimodal variation with rainfall peaks at the first and last trimester of each year. The flood extent and water height follow the rainfall regime with a time lag of 45 and 30 days, respectively ($r = 0.77$ with a lag of 20 days).
- The Ubangui subbasin presents a small dry season in the rainfall regime. This might lead to the observed plateau phase in the flood extent. That flood extent varies little within the rainfall season whereas the water height presents a small lag with the flood extent. The water height peak is within a month of the end of the flood extent plateau phase.
- The Tumba subbasin presents a wet climate with a small dry season during July-August. The flood occurs during 100 days with a maximum extent in November, synchronic with the water height peak ($r = 0.91$).

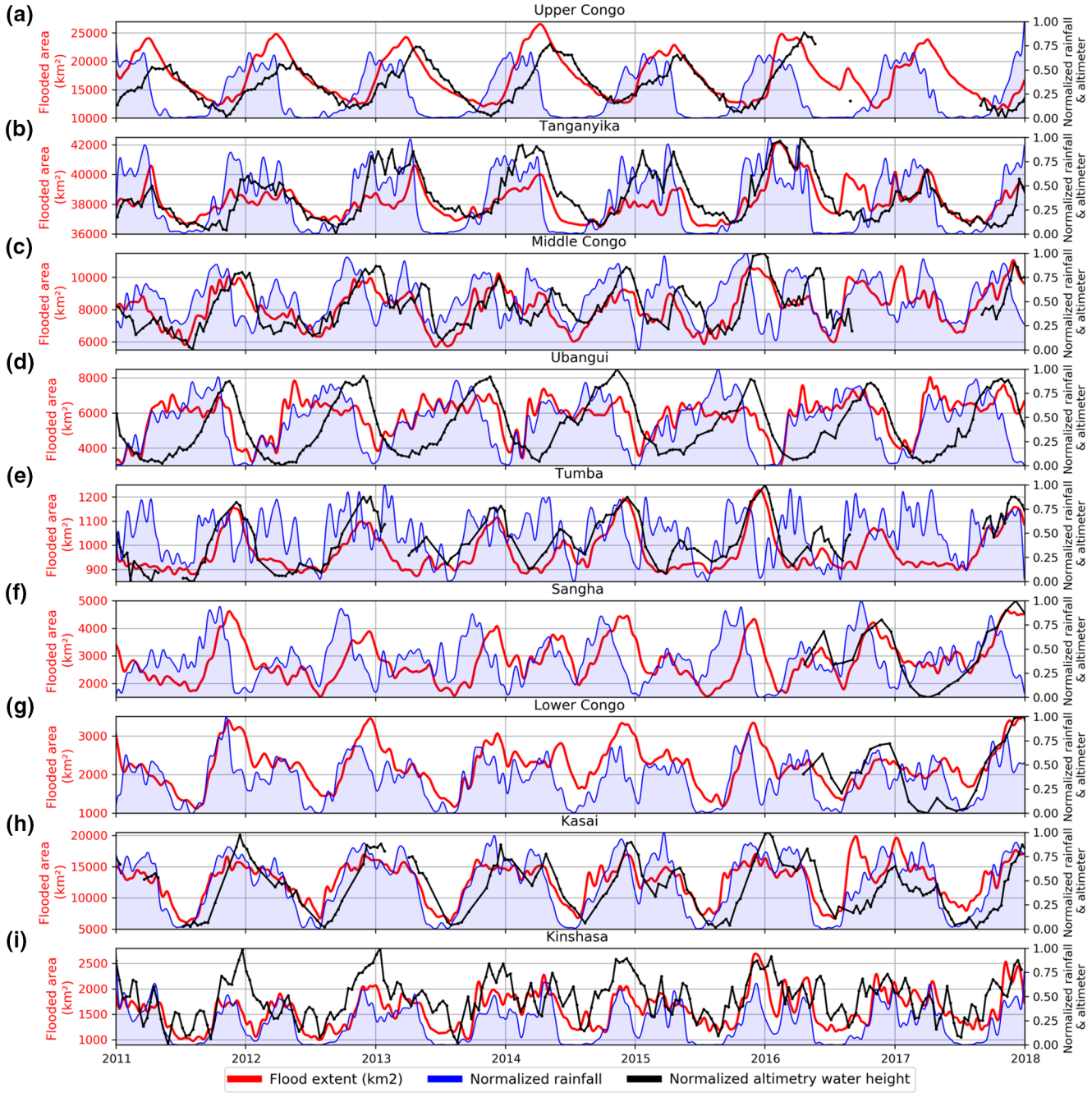

Figure 7. Time series of the total flooded area derived from SWAF (red), the normalized total rainfall from TRMM 3b42v7 data set (blue), and the normalized water height elevation (black) of the subbasin outlet altimetry height station. SWAF, Surface WAter Fraction; TRMM, Tropical Rainfall Measuring Mission.

- The Sangha subbasin presents a bimodal rainfall regime, with a first wet season from February to June, and the second from August to November. Between those rain seasons and the flood extent, there is a mean lag of about 50 days, with the maximum flood extent reached in November. The correlation between the flood extent and the water height at the outlet reaches 0.80.
- The Lower Congo subbasin present a long rainy season, and a short dry season during July-August. Its peak of flood extent is in average in December, in the middle of the rainy season. No specific relation between flood extent and water height at the outlet can be determined from these time series.

Table 2
Mean, Minimum, and Maximum Water Extent Over the Congo River Basin (CRB) for the Considered Data Sets

Data set	Mean surface (km^2)	Minimum water extent (km^2)	Maximum water extent (km^2)
SWAF	89,408	78,602	99,225[a]
ESA-CCI	70,620	—	—
SWAMPS	46,273	—	—
Global Surface Water Occurrence	75,645	—	—
IGBP	50,712	—	—

[a]The maximum surface for SWAF is 119,874 if the surfaces are summed up considering the peak date for each subbasin.

Abbreviations: CCI, Climate Change Initiative; ESA, European Space Agency; GSWO, Global Surface Water Occurrence; IGBP, International Geosphere-Biosphere Programme; SWAMPS, Surface Water Microwave Product Series

- The Kasai subbasin presents a long rainy season, and a short dry season during July-August. The flood extent is synchronous with to the rainfall regime ($r = 0.86$). The water height variation presents mostly a bimodal behavior, with a first peak in December, and a second peak in April. The lag between the flood extent and the water height peak is of 29 days (lag of 29 days leads to $r = 0.76$).
- The Kinshasa subbasin presents a 200-days long rainy season extending from September to March. The flooded area is relatively small compared to the other subbasins and concentrated on the banks of the river and the Eastern part. The flooding dynamics is highly correlated to the precipitation ($r = 0.83$). The water height peak happens in average 15 days after the flood extent peak.

The lengths of the rainy and flooding seasons have been measured for each subbasin. To such an aim, start and end of each season from the TRMM and SWAF time series have been detected. The threshold of detection has been determined from the minimum value of the whole time series plus 1.5 times the standard deviation value. The rainy and flood season lengths, along with the lag between rainfall, flood extent, and water height at the outlet have been displayed in Figure 8.

Following the threshold criterion, the longest rainy season occurs in the Middle Congo subbasin, which corresponds to the tropical rain forest extent mostly. The shortest occurs in the Upper Congo basin. The longest flood happens in the Ubangui subbasin and the shortest in the Tanganyika and Tumba subbasins. As expected, the duration of the flood season does not correspond directly to the length of the rainy season. Furthermore, due to the difference in size of each subbasin (from 14,083 to 973,778 km^2), different regimes within a subbasin may have different impacts on flooding. The month of maximum flood extent from the SWAF water fractions for the whole 2011–2017 period is displayed in Figure 9. Results have been filtered with a majority (also known as mode) filter of size 9. This filter generalizes and reduces single pixel misclassifactions (Davies, 1988).

The Upper CRB, East Tanganyika, South Middle CRB, and northern Ubangui parts of their subbasins present maximum flood extent in the first half of the year. In particular, it presents an emphasis on the January-March period in the south of the Congo basin, and in April-June for the North Congo basin (Uban-

Table 3
Lag Between Rainfall and Flood Extent, and Between Flood Extent and the Water Height Level at the Outlet of Each Subbasin

	Rainfall and flood extent		Flood extent and sub-basin outlet water height		Proportion of flooded area for 2011–2017	
Subbasin	Time lag (days)	Lagged correlation	Time lag (days)	Lagged correlation	Min. (%)	Max. (%)
Upper Congo	67	0.89	28	0.90	2.55	5.86
Tanganyika	26	0.70	5	0.68	13.69	15.81
Middle Congo	28	0.53	20	0.77	0.58	1.14
Ubangui	8	0.73	60	0.56	0.42	1.24
Tumba	41	0.34	1	0.91	6.19	8.73
Sangha	49	0.68	1	0.80	0.53	1.64
Lower Congo	23	0.76	7	0.68	1.65	5.31
Kasai	0	0.86	29	0.76	0.68	2.22
Kinshasa	0	0.83	10	0.56	0.95	2.63

The time lag is indicated (in days), along with the corresponding correlation coefficient. The proportion of minimum/maximum flooded area for the whole 2011–2017 period is also indicated.

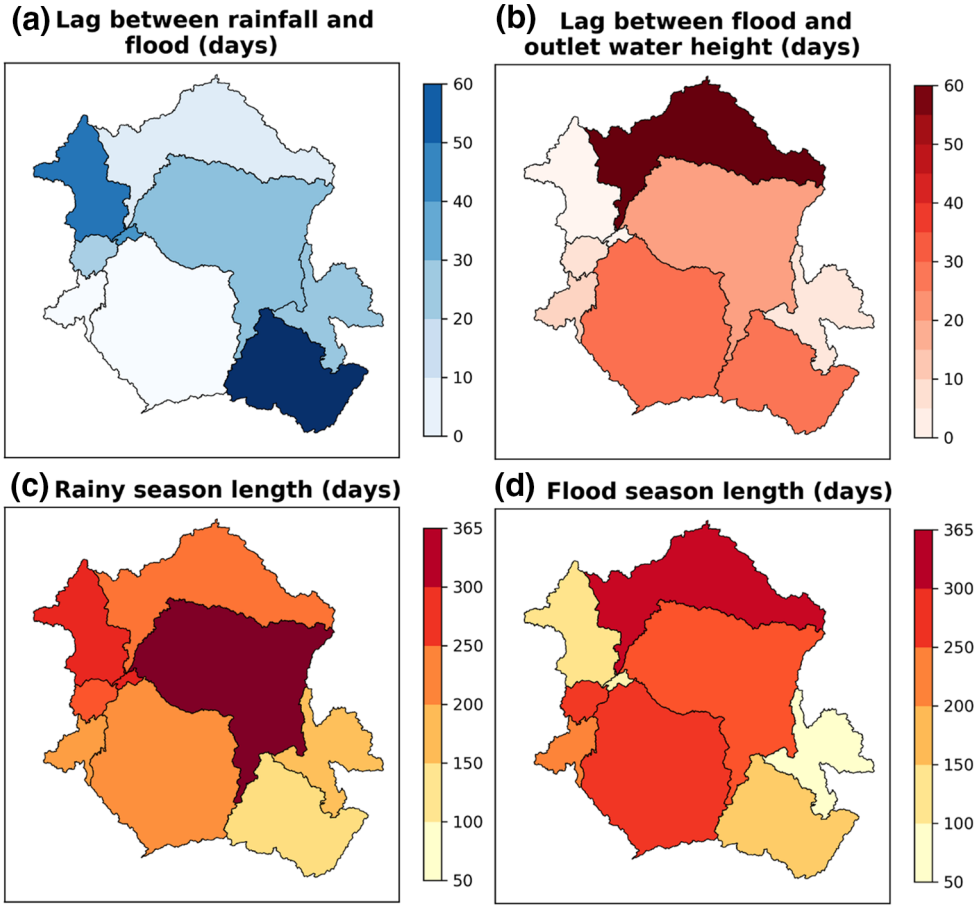

Figure 8. Hydrological indicators over the Congo River Basin: (a) lag between rainfall and flood, (b) lag between flood and outlet water height, (c) rainy season length, (d) flood season length. CRB, Congo River Basin.

gui subbasin). Conversely, the West Tanganyika, West Middle Congo, South Ubangui and Sangha, Tumba, Lower Congo, Kasai and Kinshasa subbasins present maximum extents in the second half of the year. In particular, it presents a strong emphasis for the November-December months in the Cuvette Centrale area, which presents the most noticeable floods.

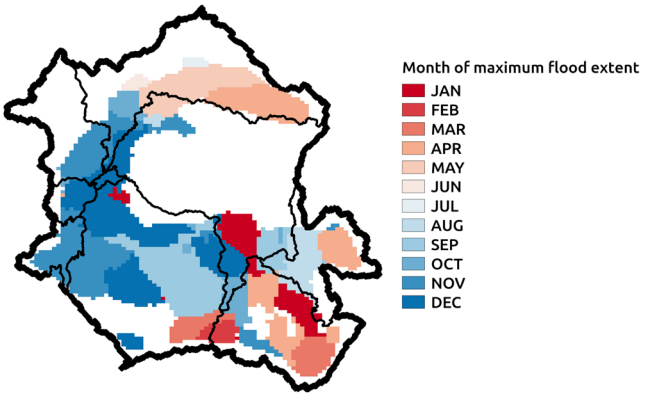

Figure 9. Map of the month corresponding to the maximum flooded areas over the Congo River Basin after the application of a majority filter of size 9.

6. Discussion

As shown in Figure 5, the detection of extreme events using surface extent provides reliable information about the drought and floods during the last decade at the subbasin scale. The annual flood already mentioned in Section 5.1 Southwest of the city of Kindu were not depicted by the other data sets used in the comparison section of the paper. This is an important point, as these yearly floods can lead to disastrous impacts in this area. For instance, >3,600 people were made homeless in November 2015 due to important floods after an abnormally dry beginning of year (UN OCHOA, 2015). This is concordant with the time series of the Middle Congo basin observed in Figure 5. This observation can be made due to the increased temporal information and sensibility of the observation-based product developed in this study. The temporal information is gained by the 3 days revisits of the SMOS sensor (Kerr et al., 2010) and

the sensibility due to the use of L-band radiometry which enables depiction of water surfaces in Tropical environment (Parrens et al., 2017).

The month of maximum flood extent (Figure 9) for each subbasin of CRB provides new observation-based knowledge of the water dynamics. The CRB can be divided from this information into two big systems. The upstream part with a maximum extent in the first five months of the year and the downstream part with a maximum extent in the last 5 months of the year. In particular, the very important flood area of the Cuvette Centrale is mostly flooded in December, with a ~20 days lag compared with the rainfall for the Lower Congo subbasin and a ~40 days lag for the Tumba subbasin. O'loughlin et al. (2013) showed the complexity of the determination of river flow dynamics in the central part of the CRB and the need for inclusion of hydraulic constraints in the modeling which were not present in previous studies (Beighly et al., 2011; Lee et al., 2011). The results from the current study confirm the complexity of the processes and provide additional tools to constrain the river modeling. The positions of the five constraints determined in O'loughlin et al. (2013) which can induce backwaters correspond to high dynamics of water surfaces. In his book, Robert et al. (1946) defined from a topogeological point of view the Cuvette Centrale as the central concave depression of the interior plateau of the CRB with an altitude lower than 500 m. Bwangoy et al. (2010) estimated the wetland area at 359,556 km^2 (31.79%) of the 1,176,000 km^2 total area of the Cuvette Centrale. In our study, we associate the wetlands of the Cuvette Centrale based on the month of maximum flood extend as shown in Figure 9. Considering this approach, this area covers 332,620 km^2 (28.28%) of the Cuvette Centrale which is quite close to the previous evaluations.

Tropical climate is characterized by a high spatial and temporal variability compared to temperate climate (Wohl et al., 2012). Consequently, the change in response of climate and anthropogenic alterations is rapid. In the CRB, the hydrological processes need to be studied with a high temporal sampling. This study focuses on the high temporal dynamic of the water surface extent component leading to a better temporal knowledge of this reservoir. The link between rainfall and water surface extent is also complex in the CRB due to the complex drainage systems and geomorphological and hydraulic properties. Ndehedehe et al. (2019) mention that runoff and evapotranspiration of each subbasin are also significant triggers of hydrological conditions other than rainfall. As shown in the results of Figures 7–9, the link between water surface extent, discharge, and rainfall is not homogeneous within a subbasin and highly differs from one subbasin to another.

The dearth of flood extent information over the Congo basin—the lack of reliable water extent dynamics products over Congo over the 2010s—is partially filled with the suggested methodology and resulting maps in this study. The use of L-band microwave SWAF extends the scope of estimation of the water surface extent in the Congo tropical basin. The water extents presented in this study were compared to the available remote sensing-based maps and dynamic products. Some products are static maps that cannot account for the dynamics in the area (for instance GSWO, IGBP, and ESA-CCI water bodies' products). Other products do not cover the area for the 2010s (SWAMPS is only available until 2013). In general, SWAF detects larger water extents surface over the whole Congo basin. Still, an underdetection of water surfaces with SWAF compared to GSWO and ESA-CCI in particular along the main rivers and lake borders (see Figure 6). This might be explained by three different factors. The first one is that the signal over water bodies can be contaminated by the adjacent soil through the Gibbs effect (Al Bitar et al., 2012). The second factor is that the reference brightness temperature for water bodies could be slightly erroneous as it relies on the physical Klein and Swift (1977) model. The Tskin estimation from ECMWF used could lead to a negative bias in water fraction. The last factor is the land cover close to river and lake borders. It is indeed, in the Congo river case, a complex mosaic of water surfaces, crop fields, low vegetation, and sparse forests. As each SMOS pixel represents a large 625 km^2 area, a slight overestimation of the soil fraction or a too low TBs compared to reality can lead to a lower SWAF estimation in these complex areas.

Over the whole CRB, the minimum SWAF flood extent reaches 78,602 km^2 and the maximum extent 99,225 km^2 between 2011 and 2017. The SWAF minimum extent is slightly over the 72,600 km^2 observed in Becker et al. (2018), when the SWAF maximum value is below the 111,532 km^2 proposed. The difference in the maximum extent is due to the methodology used: in our case, the maximum value corresponds to the maximum extent observed over the whole CRB for 2011–2017, when in Becker et al. (2018) they summed the maximum extents of each subbasin for 1993–2007. Following their methodology, we get a maximum

extent of 119,874 km^2. We have coherent values for the 2010s compared to the 1993–2007 time period of the GIEMS data, although slightly higher by a 6,000–8,000 km^2. Additionally, even though the used retrieval algorithm relies on multiangular and dual polarization, it remains dependent on the reference map for homogeneous surface components. The choice of ancillary data can induce uncertainties and bias in the estimates. For instance, using the ESA-CCI land cover may induce errors in the south western part of the CRB corresponding to the Angola compared to the well mapped as the Democratic Republic of Congo. This is more relevant when the needed reference information of homogeneous surfaces is modeled over distant location from where the retrieval is done. Also, the use of the modeled physical temperature of the water bodies may induce negative bias. Finally, the current product is at a high temporal resolution but coarse spatial resolution and it would profit from a downscaling approach similar to the SWAF Amazon application (Parrens et al., 2019), but this would require also a preliminary analysis of the digital elevation products is needed before.

7. Conclusion

The dynamics of the water surfaces over the CRB from 2010 to 2017 were analyzed with innovative remote sensing-based water fraction maps. The water surface dynamics show strong variability over the different subbasins of the Congo river for several hydrological information: lag with precipitation, flood duration, and maximum flood extent. A lag of 67 days between rainfall and inundation were found in the Upper Congo with a correlation value equal to 0.89, whereas no lag was detected in the Kasai subbasin with a correlation value equal to 0.86. It was also found that the duration of the rainy season is very different from the duration of the flood season. The temporal contribution to each floodplains and wetlands linked to the Congo discharge was evaluated. The month of maximum flood extent for each subbasin was determined. It varies from January to April for upstream subbasins and from September to December for downstream subbasin. Furthermore, a flood extent-based definition of the Cuvette Centrale is proposed in the paper which supplement the existing definitions based on river hydrology and vegetation.

These results were made possible using L-band radiometric data which can provide water surface dynamics under vegetated areas. Thus, the spatial and temporal dynamics of wetlands, peatlands, and floodplain under the second largest tropical forest of the world can be analyzed. Extreme events such as the 2014 flood in the Upper Congo, Tumba, Sangha, and Lower Congo subbasins and the winter 2016–2017 drought in the same subbasins were detected.

To achieve this the SWAF methodology already developed over the Amazon basin was adapted to the CRB considering the differentiated contribution of soil, water, and forest covers using the polarization and angular information from the SMOS data. The obtained water surfaces were compared to three independent land cover maps (ESA-CCI, IGBP, and GSWO) prior to the hydrological analysis. It was found that, on average, more water surface extent was detected with the SWAF data. Along the rivers, less water was detected than IGBP and GSWO whereas in floodplains, wetlands, and peatlands, more water was observed. SWAF data were also compared to SWAMPS and it was found that SWAF detects more inland water than SWAMPS. Future studies should address the comparison of the current data set to outputs from regional hydrodynamic models like Fleischmann et al. (2020) where the water surface products from EO were compared to 1D and 2D versions of the MGB-IPH model. This would be a preliminary analysis prior to implementation of assimilation techniques.

Further work is planned to add the current advancements into a broader context where the volume and stream flow will be considered. This will be achieved using altimetry data from existing sensors Sentinel-3 and future missions, namely SWOT. The combined use of altimetry data over low vegetated areas with the disaggregation approach suggested in Parrens et al. (2019) may enable the monitoring of water storage terms. This would be justified by the low slope in the tropicals wetlands and the linear relation between water height and water volume in these conditions.

Data Availability Statement

The SMOS products were provided by CNES and IFREMER through the CATDS-SMOS center. All data used in this study are publicly available with an open license for noncommercial use and they were all last accessed on October 10, 2020. Hydrological subbasins data set is available at https://hydrosheds.org/downloads. TRMM 3B43 data set is available at https://disc.gsfc.nasa.gov/datasets/TRMM_3B43_7370. ESA-CCI land cover maps data set is available at http://www.esa-landcover-cci.org/.ECMWF ERA5 data set is available at https://www.ecmwf.int/en/forecasts/datasets. GSWO data set is available at https://global-surface-water.appspot.com/. SWAMPS data set is available at https://iridl.ldeo.columbia.edu/SOURCES/.NASA/.JPL/.wetlands/.dailyinundation/.swamps_v3p1/. IGBP data set is available at http://www.igbp.net/. Altimetry data are available at http://hydroweb.theia-land.fr/.

Acknowledgments
This work was funded by the program Terre Océan Surfaces Continentales et Atmosphere (TOSCA) and the SWOT-Downstream program by CNES. The authors would like to thank ECMWF, NASA, CNES, and Hydroweb for data availability.

References

Abril, G., Martinez, J. M., Artigas, L. F., Moreira-Turcq, P., Benedetti, M. F., Vidal, L., et al. (2014). Amazon River carbon dioxide outgassing fuelled by wetlands. *Nature*, *505*, 395–398.

Al Bitar, A., Leroux, D., Kerr, Y. H., Merlin, O., Richaume, P., Sahoo, A., & Wood, E. F. (2012). Evaluation of SMOS soil moisture products over continental US using the SCAN/SNOTEL network. *IEEE Transactions on Geoscience and Remote Sensing*, *50*(5), 1572–1586.

Al Bitar, A., Mialon, A., Kerr, Y., Cabot, F., Richaume, P., Jacquette, E., et al. (2017). The global SMOS Level 3 daily soil moisture and brightness temperature maps. *Earth System Science Data*. *9*(1), 293–315. https://doi.org/10.5194/essd-2017-1

Alsdorf, D., Beighley, E., Laraque, A., Lee, H., Tshimanga, R., O'Loughlin, F., et al. (2016). Opportunities for hydrologic research in the Congo Basin. *Reviews of Geophysics*, *54*, 378–409. https://doi.org/10.1002/2016RG000517

Becker, M., Papa, F., Frappart, F., Alsdorf, D., Calmant, S., Santos da Silva, J., et al. (2018). Satellite-based estimates of surface water dynamics in the Congo River Basin. *International Journal of Applied Earth Observation and Geoinformation*, *66*, 196–209.

Beighley, R. E., Ray, R. L., He, Y., Lee, H., Schaller, L., Andreadis, K. M., et al. (2011). Comparing satellite derived precipitation datasets using the Hillslope River Routing (HRR) model in the Congo River Basin. *Hydrological Processes*, *25*, 3216–3229. https://doi.org/10.1002/hyp.8045

Bele, Y., Mulotwa, E., Bokoto de Semboli, B., Sonwa, D., & Tiani, A. M. (2010). *Les effets du changement climatique dans le Bassin du Congo; la nécessité de soutenir les capacités adaptatives locales*. Retrieved from https://www.semanticscholar.org/paper/Afrique-centrale-%3A-les-effets-du-changement-dans-le-Bele-Mulotwa/8b17a3f7d0e998e96c608331612bfa9bf6721de1

Birkett, C. M., & Beckley, B. (2010). Investigating the performance of the Jason-2/OSTM radar altimeter over lakes and reservoirs. *Marine Geodesy*, *33*, 204–238.

Bontemps, S., Defourny, P., Radoux, J., Van Bogaert, E., Lamarche, C., Achard, F., et al. (2013). Consistent globalland cover maps for climate modelling communities: Current achievements of the ESA's land cover CCI. In *Proceedings of the ESA living planet symposium* (pp. 9–13), Edimburgh, UK.

Broxton, P. D., Zeng, X., Sulla-Menashe, D., & Troch, P.A. (2014). A global land cover climatology using MODIS data. *Journal of Applied Meteorology and Climatology*, *53*, 1593–1605.

Bultot, F. (1974). *Atlas climatique du bassin zaïrois. Quatrième partie: Pression atmosphérique, vent en surface et en altitude, température et humidité de l'air en altitude, nébulosité et visibilité, propriétés chimiques de l'air et des précipitations et classifications cl*. Brussels:I.N.E.A.C: 193 Maps.

Bwangoy, J.-R. B., Hansen, M. C., Roy, D. P., De Grandi, G., & Justice, C. O. (2010). Wetland mapping in the Congo Basin using optical and radar remotely sensed data and derived topographical indices. *Remote Sensing of Environment*, *114*(1), 73–86. https://doi.org/10.1016/j.rse.2009.08.004

Chew, C., Reager, J. T., & Small, E. (2018). CYGNSS data map flood inundation during the 2017 Atlantic hurricane season. *Scientific Reports*, *8*, 9336. https://doi.org/10.1038/s41598-018-27673-x

Creese, A., & Washington, R. (2016). Using qflux to constrain modeled Congo Basin rainfall in the CMIP5 ensemble. *Journal of Geophysical Research: Atmospheres*, *121*, 13415–13442. https://doi.org/10.1002/2016JD025596

Dargie, G. C., Lawson, I. T., Rayden, T. J., Miles, L., Mitchard, E. T. A., & Page, S. E. (2019). Congo Basin peatlands: Threats and conservation priorities. *Mitigation and Adaptation Strategies for Global Change*, *24*, 669–686. https://doi.org/10.1007/s11027-017-9774-8

Dargie, G. C., Lewis, S. L., Lawson, I. T., Mitchard, E. T. A., Page, S. E., Bocko, Y. E., & Ifo, S. A. (2017). Age, extent and carbon storage of the central Congo Basin peatland complex. *Nature*, *542*, 7639–7686.

Da Silva, J. S., Calmant, S., Seyler, F., Rotunno Filho, O. C., Cochonneau, G., & Mansur, W. J. (2010). Water levels in the Amazon Basin derived from the ERS 2 and ENVISAT radar altimetry missions. *Remote Sensing of Environment*, *114*, 2160–2181.

Davies, E. R. (1988). On the noise suppression and image enhancement characteristics of the median, truncated median and mode filters. *Pattern Recognition Letters*, *7*(2), 87–97. https://doi.org/10.1016/0167-8655(88)90123-7

Donlon, C., Berruti, B., Buongiorno, A., Ferreira, M.-H., Féménias, P., Frerick, J., et al. (2012). The Global Monitoring for Environment and Security (GMES) Sentinel-3 mission. *Remote Sensing of Environment*, *120*, 37–57. https://doi.org/10.1016/j.rse.2011.07.024

Fleischmann, A. S., Paiva, R. C. D., Collischonn, W., Siqueira, V. A., Paris, A., Moreira, D. M., et al. (2020). Trade-offs between 1D and 2D regional river hydrodynamic models. *Water Resources Research*, *56*, e2019WR026812. https://doi.org/10.1029/2019WR026812

Friedl, M. A., Sulla-Menashe, D., Tan, B., Schneider, A., Ramankutty, N., Sibley, A., & Huang, X. (2010). MODIS collection 5 global land cover: Algorithm refinements and characterization of new datasets. *Remote Sensing of Environment*, *114*, 168–182.

Harris, F. J. (1978). On the use of windows for harmonic analysis with the discrete Fourier transform. *Proceedings of the IEEE*, *66*(1), 51–83. https://doi.org/10.1109/PROC.1978.10837

Huffman, G. J., Adler, R. F., Bolvin, D. T., Gu, G. J., Nelkin, E. J., Bowman, K. P., et al. (2007). The TRMM multisatellite precipitation analysis (TMPA): Quasi-global, multiyear, combined-sensor precipitation estimates at fine scales. *Journal of Hydrometeorology*, *8*(1), 38–55. https://doi.org/10.1175/JHM560.1

Huffman, G. J., Adler, R. F., Rudolf, B., & Keehn, P. R. (1995). Global precipitation estimates based on a technique for combining satellite-based estimates, rain-gauge analysis, and NWP model precipitation information. *Journal of Climate*, *8*(5), 1284–1295. https://doi.org/10.1175/1520-0442008

IPCC. (2007). *Climate change 2007: Impacts, adaptation and vulnerability. In Contribution of working group II to the fourth assessment report of the intergovernmental panel on climate change*. Cambridge, UK: Cambridge University Press.

Jung, H. C., Hamski, J., Durand, M., Alsdorf, D., Hossain, F., Lee, H., & Hoque, A. Z. (2010). Characterization of complex fluvial systems using remote sensing of spatial and temporal water level variations in the Amazon, Congo, and Brahmaputra Rivers. *Earth Surface Processes and Landforms: The Journal of the British Geomorphological Research Group*, *35*(3), 294–304.

Kerr, Y., Waldteufel, P., Wigneron, J., Martinuzzi, J., Font, J., & Berger, M. (2001). Soil moisture retrieval from space: The Soil Moisture and Ocean Salinity (SMOS) mission. *IEEE Transactions on Geoscience and Remote Sensing*, *39*, 1729–1735.

Kerr, Y. H., Waldteufel, P., Richaume, P., Wigneron, J.-P., Ferrazzoli, P., Mahmoodi, A., et al. (2012). The SMOS soil moisture retrieval algorithm. *IEEE Transactions on Geoscience and Remote*, *50*, 1384–1403.

Kerr, Y. H., Waldteufel, P., Wigneron, J. P., Delwart, S., Cabot, F., Boutin, J., et al. (2010). The SMOS mission: New tool for monitoring key elements of the global water cycle. *Proceedings of the IEEE*, *98*(5), 666–687. https://doi.org/10.1109/jproc.2010.2043032

Klein, L., & Swift, C. (1977). An improved model for the dielectric constant of sea water at microwave frequencies. *IEEE Transactions on Antennas and Propagation*, *25*, 104–111.

Laraque, A., Bellanger, M., Adèle, G., Guebanda, S., Gulemvuga, G., Pandi, A., et al. (2013). Recent evolution of Congo, Oubangui and Sangha Rivers flows. *Geo-Eco-Trop*, *37*(1), 93–100.

Laraque, A., Bricquet, J. P., Pandi, A., & Olivry, J. C. (2009). A review of material transport by the Congo River and its tributaries. *Hydrological Processes*, *23*, 3216–3224. https://doi.org/10.1002/hyp.7395

Laraque, A., Mahé, G., Orange, D., & Marieu, B. (2001). Spatiotemporal variations in hydrological regimes within Central Africa during the XXth century. *Journal of Hydrology*, *245*, 104–117.

Lavalle, M., Morris, M., Shah, R., Zuffada, C., Nghiem, S. V., Chew, C., & Zavorotny, V. U. (2018). Bistatic scattering modeling for dynamic mapping of tropical wetlands with CYGNSS. In *IGARSS 2018 IEEE international geoscience and remote sensing symposium*, (pp. 239–242), Valencia. https://doi.org/10.1109/IGARSS.2018.8519285

Lee, H., Beighley, R. E., Alsdorf, D., Jung, H. C., Shum, C. K., Duan, J., et al. (2011). Characterization of terrestrial water dynamics in the Congo Basin using GRACE and satellite radar altimetry. *Remote Sensing of Environment*, *115*(12), 3530–3538. https://doi.org/10.1016/j.rse.2011.08.015

Lee, H., Jung, H. C., Yuan, T., Beighley, R. E., & Duan, J. (2014). Controls of terrestrial water storage changes over the central Congo Basin determined by integrating PALSAR ScanSAR, Envisat altimetry, and GRACE data. *Remote Sensing of the Terrestrial Water Cycle*, *206*, 117.

Lee, H., Yuan, T., Jung, H. C., & Beighley, E. (2015). Mapping wetland water depths over the central Congo Basin using PALSAR ScanSAR, Envisat altimetry, and MODIS VCF data. *Remote Sensing of Environment*, *159*, 70–79.

Lehner, B., Verdin, K., & Jarvis, A. (2008). New global hydrography derived from spaceborne elevation data. *Eos, Transactions American Geophysical Union*, *89*, 93–95. https://doi.org/10.1029/2008EO100001

Mayaux, P., De Grandi, G., & Malingreau, J. P. (2000). Central African forest cover revisited: A multisatellite analysis. *Remote Sensing of Environment*, *71*, 183–196.

Mayaux, P., De Grandi, G., Rauste, Y., Simard, M., & Saatchi, S. (2002). Large-scale vegetation maps derived from the combined L-band GRFM and C-band CAMP wide area radar mosaics of Central Africa. *International Journal of Remote Sensing*, *23*(7), 1261–1282.

Munzimi, Y. A., Hansen, M. C., & Asante, K. O. (2019). Estimating daily streamflow in the Congo Basin using satellite-derived data and a semi-distributed hydrological model. *Hydrological Sciences Journal*, *64*(12), 1472–1487.

Ndehedehe, C. E., Anyah, R. O., Alsdorf, D., Agutu, N. O., & Ferreira, V. G. (2019). Modelling the impacts of global multi-scale climatic drivers on hydro-climatic extremes (1901–2014) over the Congo basin. *The Science of the Total Environment*, *651*, 1569–1587.

O'loughlin, F., Trigg, M. A., Schumann, G. P., & Bates, P. D. (2013). Hydraulic characterization of the middle reach of the Congo River. *Water Resources Research*, *49*, 5059–5070. https://doi.org/10.1002/wrcr.20398

Papa, F., Güntner, A., Frappart, F., Prigent, C., & Rossow, W. B. (2008). Variations of surface water extent and water storage in large river basins: A comparison of different global data sources. *Geophysical Research Letters*, *35*, L11401. https://doi.org/10.1029/2008GL033857

Parrens, M., Al Bitar, A., Frappart, F., Paiva, R., Wongchuig, S., Papa, F., et al. (2019). High resolution mapping of inundation area in the Amazon basin from a combination of L-band passive microwave, optical and radar datasets. *International Journal of Applied Earth Observation and Geoinformation*, *81*, 58–71. https://doi.org/10.1016/j.jag.2019.04.011

Parrens, M., Al Bitar, A., Frappart, F., Papa, F., Wigneron, J.-P., & Kerr, Y. (2017). Mapping dynamic water fraction under the tropical rain forests of the Amazonian basin from L-band brightness temperature. *Water*, *9*(5), 350.

Pekel, J. F., Cottam, A., Gorelick, N., & Belward, A. S. (2016). High-resolution mapping of global surface water and its long-term changes. *Nature*, *540*, 418–422.

Pham-Duc, B., Prigent, C., Aires, F., & Papa, F. (2017). Comparisons of global terrestrial surface water datasets over 15 years. *Journal of Hydrometeorology*, *18*, 993–1007.

Prigent, C., Matthews, E., Aires, F., & Rossow, W. (2001). Remote sensing of global wetland dynamics with multiple satellite data sets. *Geophysical Research Letters*, *28*, 4631–4634.

Prigent, C., Papa, F., Aires, F., Rossow, W., & Matthews, E. (2007). Global inundation dynamics inferred from multiple satellite observations, 1993–2000. *Journal of Geophysical Research*, *112*, D12107. https://doi.org/10.1029/2006JD007847

Revel, M., Ikeshima, D., Yamazaki, D., & Kanae, S. (2019). A physically based empirical localization method for assimilating synthetic SWOT observations of a continental-scale river: A case study in the Congo Basin. *Water*, *11*(4), 829.

Richey, J. E., Melack, J. M., Aufdenkampe, A. K., Ballester, V. M., & Hess, L. L. (2002). Outgassing from Amazonian rivers and wetlands as a large tropical source of atmospheric CO_2. *Nature*, *416*, 617–620.

Robert, M. (1946). *Le Congo physique*. Liège, Belgium: H. Vaillant - Carmanne, S. A.

Rosenqvist, Å., & Birkett, C. M. (2002). Evaluation of JERS-1 SAR mosaics for hydrological applications in the Congo river basin. *International Journal of Remote Sensing*, *23*(7), 1283–1302.

Samba, G., Nganga, D., & Mpounza, M. (2008). Rainfall and temperature variations over Congo-Brazzaville between 1950 and 1998. *Theoretical and Applied Climatology*, *91*, 85–97.

Schroeder, R., McDonald, K. C., Chapman, B. D., Jensen, K., Podest, E., Tessler, Z. D., et al. (2015). Development and evaluation of a multi-year fractional surface water data set derived from active/passive microwave remote sensing data. *Remote Sensing*, *7*, 16688–16732.

Silva, I. A. A. D., Silva, T. M. S. D., Camara, C. A., Queiroz, N., Magnani, M., Novais, J. S. D., et al. (2013). Phenolic profile, antioxidant activity and palynological analysis of stingless bee honey from Amazonas, Northern Brazil. *Food Chemistry*, *141*(4), 3552–3558.

Soldo, Y., Khazaal, A., Cabot, F., & Kerr, Y. (2015). An RFI index to quantify the contamination of SMOS data by radio-frequency interference. *Journal of Selected Topics in Applied Earth Observations and Remote Sensing*, *99*, 1–13.

Tshimanga, R. M., & Hughes, D. A. (2014). Basin-scale performance of a semi distributed rainfall-runoff model for hydrological predictions and water resources assessment of large rivers: The Congo River. *Water Resources Research*, *50*, 1174–1188. https://doi.org/10.1002/2013WR014310

Ulaby, F. T. (1982). Microwave remote sensing: Active and passive. In Radar remote sensing and surface scattering and emission theory (Vol. 2). Reading, MA: Addison-Wesley.

Ulaby, F. T., Allen, C. T., & Fung, A. K. (1983). Method for retrieving the true backscattering coefficient from measurements with a real antenna. *IEEE TGRS*, *21*(3), 308–313. https://doi.org/10.1109/TGRS.1983.350558

UN OCHOA (2015). *UN Office for the Coordination of Humanitarian Affairs.* DR Congo: Floods. Retrieved from https://www.humanitarianresponse.info/fr/disaster/fl-2015-000164-cod

Vanden Bossche, J. P., & Bernacsek, G. M. (1990). Source book for the inland fishery resources of Africa (Vol. 1, pp. 338–339).Rome, Italy: Food and Agriculture Organization of the United Nations.

Verhegghen, A., Mayaux, P., de Wasseige, C., & Defourny, P. (2012). Mapping Congo Basin vegetation types from 300 m and 1 km multi-sensor time series for carbon stocks and forest areas estimation. *Biogeosciences*, *9*(12), 5061–5079. https://doi.org/10.5194/bg-9-5061-2012

Washington, R., James, R., Pearce, H., Pokam, W. M., & Moufouma-Okia, W. (2013). Congo Basin rainfall climatology: Can we believe the climate models? *Philosophical Transactions of the Royal Society B: Biological Sciences*, *368*(1625), 20120296.

Wohl, E., Barros, A., Brunsell, N., Chappell, N. A., Coe, M., Giambelluca, T., et al. (2012). The hydrology of the humid tropics. *Nature Climate Change*, *2*(9), 655.